ZANCO Journal of Pure and Applied Sciences
The official scientific journal of Salahaddin University-Erbil
https://zancojournals.su.edu.krd/index.php/JPAS

ISSN (print):2218-0230**, ISSN (online):** 2412-3986**, DOI: http://dx.doi.org/10.21271/zjpas**

RESEARCH PAPER

Synthesis of liquid crystalline benzothiazole based derivatives: Theoretical and experimental study of their optical and electrical properties

Shalaw K. Salih[1], Rebaz M. Mustafa[1,2], Dyari M. Mamad[3], Kosrat N. Kaka[1*], Rebaz A. Omer[1], Wali M. Hamad[1]

[1]Department of Chemistry, Faculty of Science & Health, Koya University, Koya KOY45, Kurdistan Region – F.R. Iraq.

[2]Volumetric Apparatus and Instrumental Analysis, Modern Surveying Calibration & Testing Labs, Erbil, Kurdistan, Iraq.

[3]University of Raparin, College of Science, Department of Physics, Sulaymaniyah, Iraq

A B S T R A C T:

This study describes the synthesis of 2,5-Bis(3,4-dialkoxy phenyl) Thiazolo[5,4-d} thiazoles (DAITn) (I) and its subsequent structural analysis. These compounds were prepared via reaction of dithio-oxarnidc with the freshly prepared 3,4-dialkoxy benzaldehyde in (DMF). The structure of DAITn (I) was found to have the 3 and 4 positions of the two benzene rings substituted with (OCnH2n+h n=2-5) which equaled to compound M2-M5. The primary methods used for theoretical calculations in this study are quantum mechanics/molecular dynamics simulations based on Density Functional Theory (DFT) and Monte Carlo. The Gaussian09W software's B3LYP hybrid feature and 6-311++G(d,p) basis set were employed in both the gas and aqueous phase for protonated and non-protonated species at the B3LYP level. Electronic structural identifiers were discovered from geometry-optimized structures and correlations between EHOMO (higher occupied molecular orbital energy), ELUMO (lower unoccupied molecular orbital energy), (Eg) bandgap energy, (I) ionization energy, (χ) electronegativity, (ΔN) electron transfer, and (ΔE_(b-d)) back-donation energy were calculated. The Monte Carlo method was used to calculate the adsorption for all identified compounds in this study, and a Fe (110) crystal more stable surface was selected. UV-visible spectroscopy is measuring absorption coefficient, transmittance, and electrical conductivity, and uses a Tauc plot for bandgap energy of the highest absorption peaks. ADTTn molecules with a wide bandgap and a high optical conductivity. Thermodynamic parameters, molecular dynamics simulations, and adsorption energy have been examining inhibitor/surface interactions with greater binding energy leading to stronger interaction and larger negative adsorption energy value indicating a more stable interaction. A four-slab model featuring eighty iron atoms per layer, or one hundred- and ten-unit cells, was used, along with a spline transformation function and a cut-off distance of 1.85 nm for nonbonded interactions. Simulated heating was employed to progressively lower the temperature and search for a low-energy adsorption site.

KEY WORDS: Synthesis, DFT, Monte Carlo, B3LYP, Bandgap Energy, Ionization Energy, Electronegativity, Electron Transfer, Adsorption, Fe (110) Crystal.

DOI: http://dx.doi.org/10.21271/ZJPAS.35.5.14

ZJPAS (2023) , 35(5);143-162 .

1.INTRODUCTION :

Several heterocyclic mesomorphic compounds have been synthesized, and their mesomorphic properties have been studied in recent years (Matharu and Chambers- Asman, 2007, Gallardo et al., 2001, Seed, 2007, Hamad et al.).

This is not only due to the increased potential for novel mesogenic molecules provided by heterocyclics, but also because the incorporation of heteroatoms has a significant impact on the formation of mesomorphic phases. The presence of heteroatoms such as sulfur, oxygen, and nitrogen can significantly alter the polarity,

* **Corresponding Author:**
Sarbaz I. Mohammed
E-mail: sarbaz.mohammed@su.edu.krd

Article History:
Received: 05/03/2023
Accepted: 30/04/2023
Published: 25/10 /2023

polarizability, and even the shape of a molecule, having an impact on the type of mesophase, the transition temperature, and the dielectric and other characteristics of the mesogen (Ong et al., 2018). Incorporating heterocyclic rings such as pyridine (Petrov et al., 1995, Vardar et al., 2021, Ong et al., 2018), thiophene (Wu et al., 2000, Nafee et al., 2020, Li et al., 2020), and 1,3,4-thiadiazole (Han et al., 2008, Parra et al., 2012, Sharma et al., 2019, Tomi et al., 2021) in liquid-crystalline materials has been extensively documented.

It has been suggested from previous studies that increasing the molecular polarizability and clearing temperature of a given group of Schiff base esters by adding a lateral hydroxyl group at the ortho position increases their overall stability (Yeap et al., 2006, Teoh et al., 2022). This intramolecular hydrogen bond can also strengthen the overall stability of the molecule (Yeap* et al., 2004); however, the lateral substituents may interfere with the liquid crystalline phases or even eliminate them (Ha et al., 2009). Thus, the present study aims to explore the effect of the lateral hydroxyl group on the mesomorphic characteristics of benzothiazoles.

The DFT formalism is a standout amongst the various modeling approaches due to its ability to generate precise physicochemical properties at the microscopic level with a low cost of processing (Parlak et al., 2022). This quantum approach can be utilized to calculate frontier orbitals, nucleophilic and/or electrophilic sites, kinetics, and thermodynamic properties (Rebaz et al., 2022, Koparir et al., 2022). Additionally, DFT enables the optimization of organic molecules' geometry, IR spectra, and the creation of Frontier Molecular Orbitals (FMO) for electronic characterization and the calculation of quantum reactivity descriptors in order to understand the molecule's behavior as a nucleophile or electrophile (Omer et al., 2022c, Rebaz et al., 2022).

Liquid crystals are thermodynamically stable states which have properties that are anisotropic without the presence of a three-dimensional crystalline lattice, and typically occur in temperatures between the anisotropic solid and isotropic liquid phases (Singh, 2000). Common features of liquid crystal materials include long-axis rigidity, rod-like molecular structures and strong dipoles or readily polarizable substituents (Maurya and Awasthi, 2022). The liquid crystalline state is characterized by the alignment of molecules along a common axis, known as the director (Platschek, 2007). Nematic (N), smectic (S), and cholesteric (C) liquid crystal phases can be identified based on the degree of order in the material, depending on the mesophase structure (C). The nematic phase is distinguished in that the molecules can flow along an ordered axis in translation (Bukowczan et al., 2021).

This research aimed to assess the optoelectronic properties of organic compounds in terms of their efficiency. To do this, the structure of the molecules was calculated using B3LYP/cc-pVDZ and Monte Carlo.

2.Experimental and methods

The synthesis of 2,5-Bis(3,4-dialkoxy phenyl) Thiazolo[5,4-d} thiazoles (DAITn)(I) was completed using the technique published in work (Hamad et al. 2004). Subsequently, its molecular structure was verified through FT-IR, ^{1}H-NMR, and ^{13}C-NMR analysis, with the 3,4 positions of the two benzene rings substituted with (OCnH2n+h 0=2-5) see Figure 1.

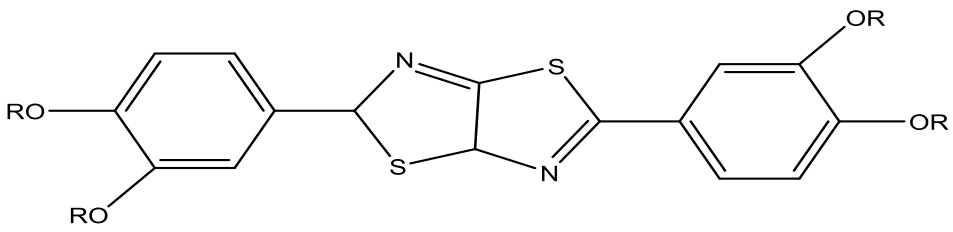

(I) DATTn (R= CnH2n+1 n=2-5, M1-M2)

Figure 1: Molecular structure of 2,5-Bis(4- alkyl phenyl) thiazolo [5,4-d]

3.Theoretical study

The principal theoretical calculation methodologies used quantum mechanics/molecular dynamics simulations based on DFT and Monte Carlo. Based on the frontier molecular orbital (FMO) theory, when investigating the chelation procedure of chemisorption, The HOMO and LUMO must be considered because the interaction between the HOMO and/or LUMO utilized to evaluate the chemical reactivity properties of the majority of chemical reactions. The most common molecular classifications for DFT-based approximation in this study at 6-311++G(d,p) basis set in both gas and aqueous phase for protonated and non-protonated species at B3LYP level are used (Mamand and Qadr, 2021, MAMAND, 2019, OMER et al., 2022b). Additionally, the hybrid feature B3LYP in the Gaussian09W software is appropriate for the number of terminals and 6-31G ++ (d, p) as the basis set. Electronic structural identifiers were discovered from geometry-optimized structures, and the correlation between E_{HOMO} (higher occupied molecular orbital energy), E_{LUMO} (lower unoccupied molecular orbital energy), (Eg) bandgap energy, (I) ionization energy, (χ) electronegativity, (ΔN) electron transfer, (ΔE_{b-d}) back-donation energy was calculated. In order to calculate the adsorption for all the identified compounds in this study the Monte Carlo method was used (Christoffersen et al., 2002, Guo et al., 2015, Omer et al., 2022a). The Fe (110) crystal surface was selected for this simulation because it is the most stable surface described in the literature. In order to mimic the Fe (110) surface, a four-slab model was employed (Erdoğan et al., 2017, Parlak et al., 2022). This model featured eighty iron atoms per layer, or one hundred- and ten-unit cells. Using a spline transformation function and a cut-off distance of 1.85 nm for nonbonded interactions (total energy, average total energy, van der Waals, electrostatic interactions, and intramolecular energy). A low-energy adsorption site determined through a Monte Carlo search of the substrate-adsorbed system's structure space while progressively lowering the temperature (simulated heating).

$$I = -E_{HOMO} \quad (1)$$

$$A = -E_{LUMO} \quad (2)$$

$$\chi = \frac{I + A}{2} \quad (3)$$

$$\eta = \frac{I - A}{2} \quad (4)$$

$$\Delta N_{max} = \frac{\chi_{Fe} - \chi_{inh}}{2\eta(\eta_{Fe} + \eta_{inh})} \quad (5)$$

$$\chi = \frac{I + A}{2} \quad (6)$$

I = Ionization energy, *A* = electronic affinity

4.Results and Discussions

4.1UV-visible spectroscopy

In chemical engineering, UV-visible spectroscopy is commonly employed to quantify analytes such as transition metal ions, strongly conjugated chemical substances, and biological macromolecules (Achar and Lokesh, 2004, Ou et al., 2006, Todoran et al., 2018). The UV-visible spectrum is used to determine the size and concentration of nanoparticles. Through the use of a UV spectrum, we can obtain some important physical parameters, one of which is the bandgap energy and refractive index, which are two important parameters in the field of optoelectronics (Aydin et al., 2019). All of the compound derivatives produced and described are quite colorful. The UV-Visible absorption spectra were obtained to determine how much visible and ultraviolet light these dyes can absorb. The absorption spectra in N, N-dimethylformamide solvent are shown in Figure 2, displayed as a function of their molar extinction coefficients. The absorption spectra demonstrate that all of the dyes can absorb light in the region of 200-430 nm. The maximum wavelength is 430 nm for compound 4 (M5). The maximum wavelength for all

compounds (M2-M5) was remarkably comparable due to the minor distinctions in their molecular structures.

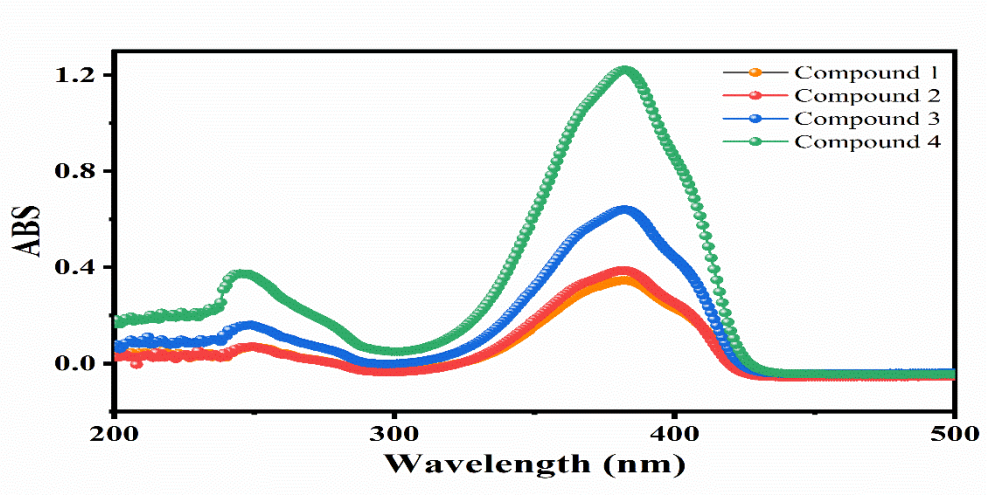

Figure 2. UV-visible spectrum of selected compounds

4.2Optical properties

Absorption is another phenomenon that may occur when light travels through an optical window. The degree of light absorption on the inside and outside of a material is the same (Akl, 2004). The absorption coefficient may be calculated using the extinction coefficient (Al-Kuhaili et al., 2012). The absorption coefficient of materials may be calculated using the Maxwell and wave equations (Orek et al., 2017).

$$\alpha = \frac{4\pi k}{\lambda} \quad (7)$$

Where k denotes the extinction coefficient, α absorption coefficient and λ is the wavelength. These coefficients influence energy losses (Shahbazi et al., 2019, Bohren and Huffman, 2008, Shan et al., 2018). The absorption of electromagnetic radiation by materials may be explained by two primary processes. (1) electrical transitions: electrons are stimulated from the valence band into unfilled energy levels in the conduction band or from the HOMO highest occupied molecular orbital to the LUMO lowest unoccupied molecule orbital. (2) Absorption: from the oscillating electric field and light, rotating vibrating and stimulating vibrational modes in the dielectric, the proportion of light transmitted may

be calculated using the following equation for a single-phase (Shan et al., 2018).

$$T = \frac{I}{I_0} = \exp(-\alpha x)$$

Intensity (I) of the transmitted radiation through a thickness (x)
I_0 = Intensity of incoming radiation.
a = Absorption coefficient of the material.

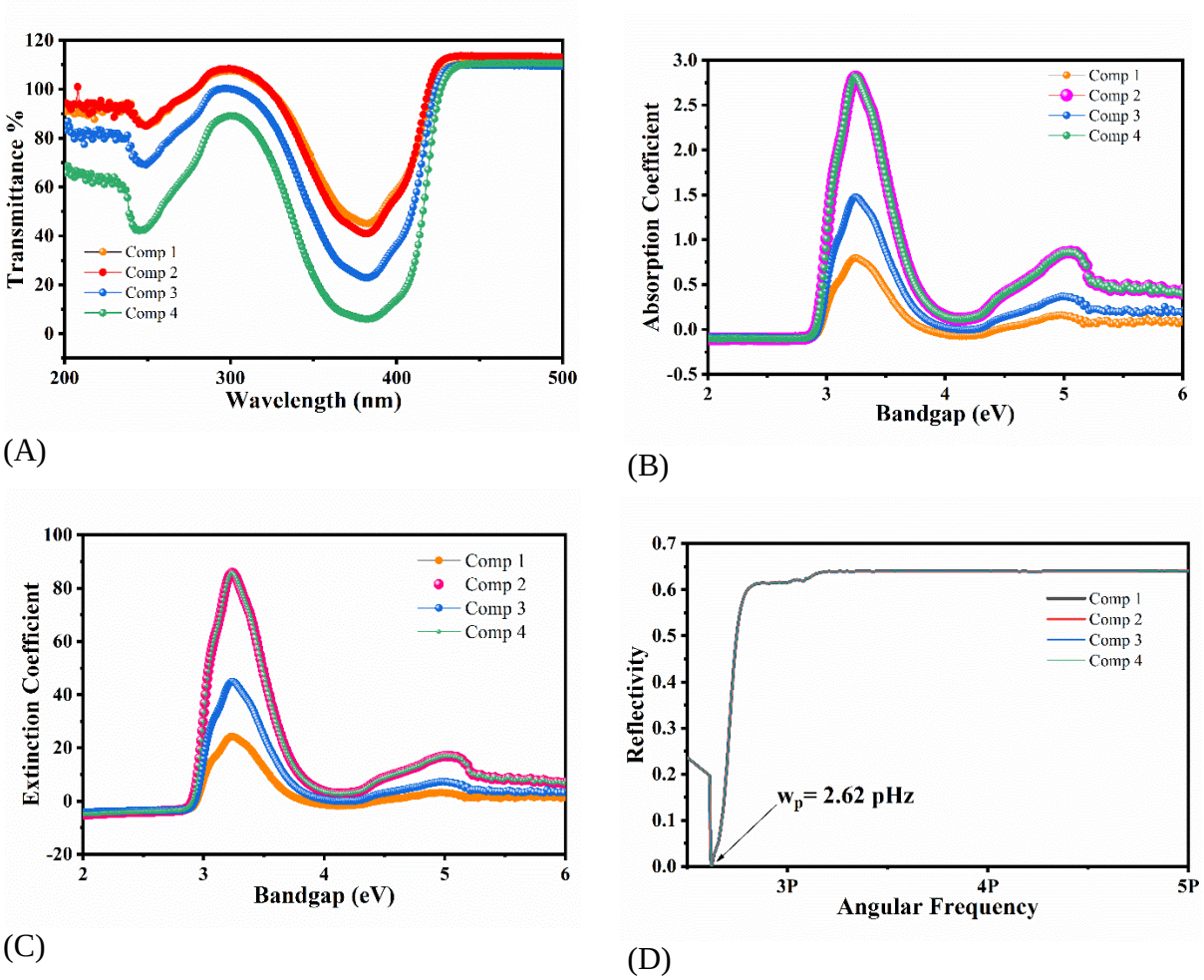

Figure 3. (A) Transmittance variation, (B) Absorption coefficient and (C) Extinction coefficient variation with energy gap, (D) Reflectivity with Angular frequency (rad s^{-1}).

The transmittance is a valuable characteristic that has a relationship with the refractive index of the materials; the importance of transmittance estimation approaches provides detailed information on the refractive index of the sample (Toft and Kvalheim, 1993). Several molecule parameters, such as concentration of the host medium, particle color, shape, impurities, sample thickness, and wavelength of light when impacting the molecule, have a strong link with light transmittance through the compounds. The highest absorption point had the lowest transmitted light as shown in Figure 3A. At wavelength 381 nm, which is equal to 3.254 eV, Materials with such high light transmission have low electrical conductivity. However, a material with high conductivity has a high reflectivity. It is feasible for a material's plasma frequency to be just below the visible frequency, allowing the material to be a strong electrical conductor while being transparent at the visible frequency. Due to the strong relationship between electrical and optical qualities. For this purpose, we can notice in Figure 3D that these materials express the plasma frequency (ω_p) in the range of 2.62 PHz. This range corresponds to maximum absorption in the UV-spectrum. The reflectivity of these materials has increased significantly from 2.62, which increases the electrical conductivity. After this range, the reflectivity reached 0.61, as shown in Figure 3D. The critical connections between the absorption coefficient, Eg of semiconductor material, and light absorption by semiconductor material may be expressed in terms of the absorption coefficient (α) on photon energy (h). The following equation can be used to compute the prohibited bandwidth of optical transitions and the optical band-gap of semiconductors.

$$(\alpha h\nu)^{m} = A^{*}(h\nu - E_g)^{m} \quad (9)$$

$\boldsymbol{E_g}$ is the energy of the optical band gap, ***n*** is the power factor of the transition mode, absorption coefficient (α) and ***(hv).*** photon energy The value of m varies depending on the type of transition; for forbidden indirect transformations, m is equal to 3, for permitting indirect transitions, m is equal to 3/2 for allowed direct transitions, and m

is equal to 1/2 for allowing a direct transfer (Orek et al., 2017). The Tauc plot is a useful tool for determining the band-gap energy associated with the highest absorption of light peaks. We calculated the allowed indirect conversion bandgap energies for all given molecules, which are shown in Figure 4 together with the value of the band gap.

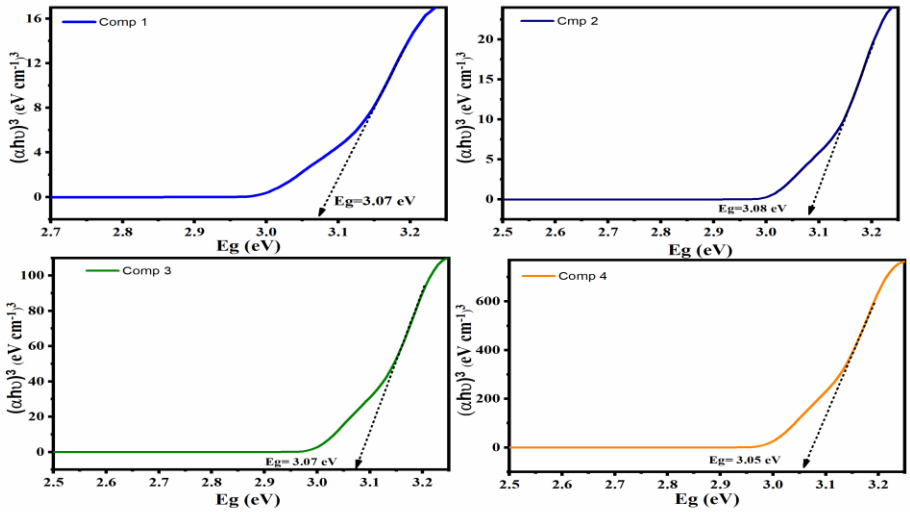

Figure 4. Tauc plot of selected compounds in this study

4.3Refractive index

Semiconductor materials have been highly sought out by optical designers for many years because of their usefulness in the production of electronic components, optoelectronic components, and photonic modulators that work in the Mid-infrared (2-5 m) range. Examples of these components are photodetectors (PDs), heterogeneous lasers, and light-emitting diodes (LEDs) (Tripathy, 2015). The refractive index and bandgap energy are two significant features of semiconductor materials, and these two qualities may be determined by their fundamental properties. The refractive index is correlated to material structure and is an indicator of transparency to incoming photons (Orek et al., 2017). Energy gap is determined by a semiconductor's photon absorption threshold. Refractive index can be calculated using equation below. Figure 5 shows that as bandgap energy increases, refractive index decreases. M4 molecule's refractive index in N, N-dimethylformamide solvent has maximum value at lowest Eg after 2.95 eV reduced up to 3.6 eV and evaluated M4 solvent line of refractive index.

$$n = \left\{ \left[\frac{4R}{(R-1)^2} \right]^{\frac{1}{2}} - \frac{R+1}{R-1} \right\} \quad (10)$$

Several relationships, such as Ravindra, Moss, Kumar and Singh, Herve and Vandame, may be used to calculate the refractive index of a semiconductor material (Epstein et al., 2009, Turan et al., 2012). These relationships are dependent on bandgap energy and are often used to calculate the n of semiconductors (Ravindra et al., 2007).

Moss relationship

$$n^4 E_g = 95\ eV$$

Reddy relation

$$n^4 (E_g - 0.365) = 154$$

Kumar and Singh relation:

$$n = KE_g^c$$

Where K and C are constants and K is 3.3668 and C is −0.32234.
Herve-Vandamme relationship:

$$n^2 = 1 + \left(\frac{A}{E_g + B}\right)^2$$

Ravindra relationship:

$$n = 4.084 + 0.62E_g$$

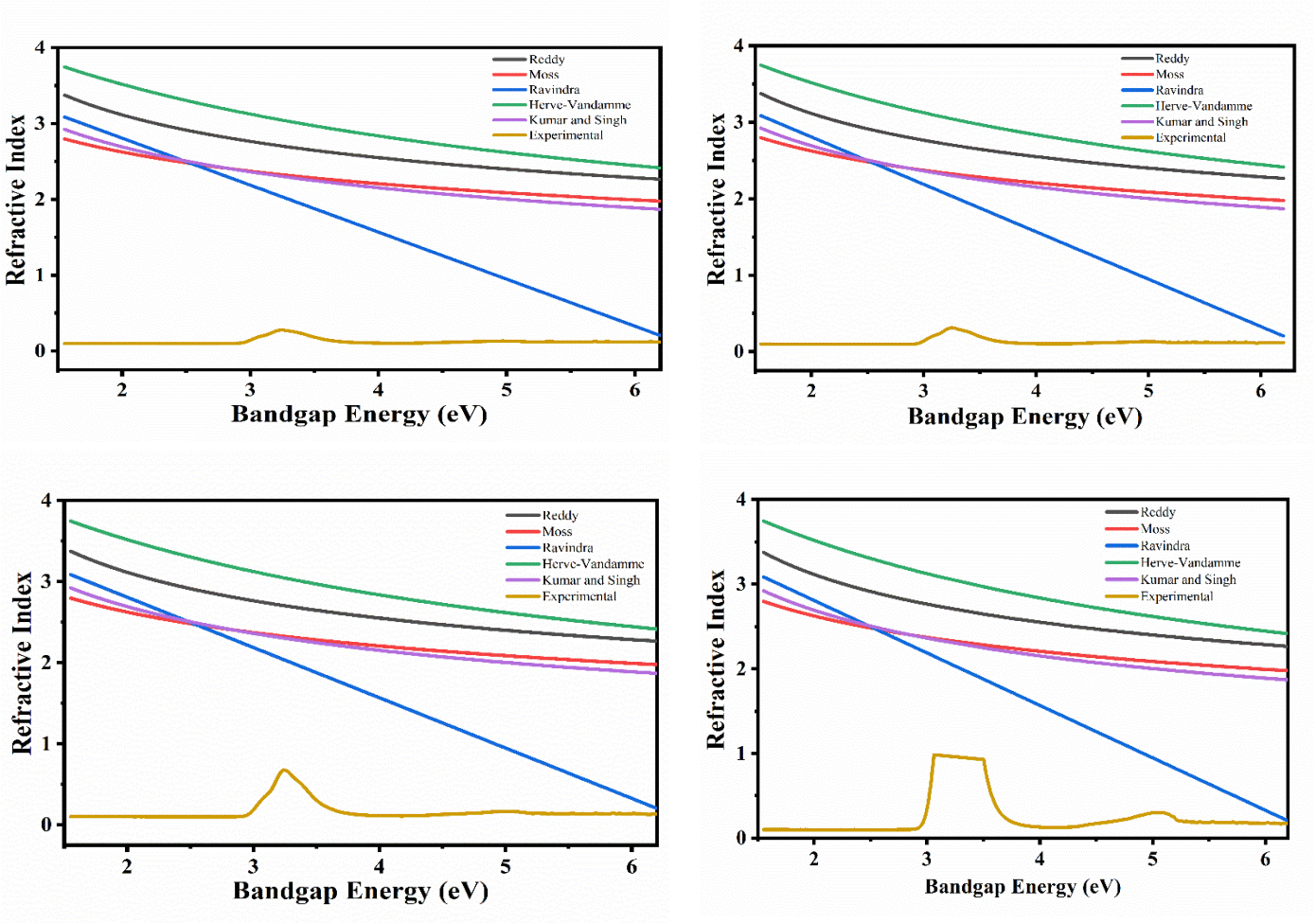

Figure 5. Refractive index with bandgap energy for M2-M5 compounds

In general, what is yellow in color expresses the shape of the refractive index for all materials. The highest range of this light refraction and band gap for each material respectively (3.24, 0.117), (3.26, 0.118), (2.95, 0.143), (3.07, 0.37). The dispersion parameter should be considered while examining the physical features of materials such as light bending and how light bends at each given wavelength. Designers create optical pigments from materials, and scattering area is a significant attribute (Mamand and Qadr, 2021). The scattering area is determined by the material's refractive index and can shift as the angular frequency rises, increasing the scattering area(Mamand et al., 2022). Dispersion is the variation in frequency caused by the refractive index. The normal dispersion regions of these materials used in this study are approximately identical in terms of frequency but with different reflectivity, as shown in Figure 6.

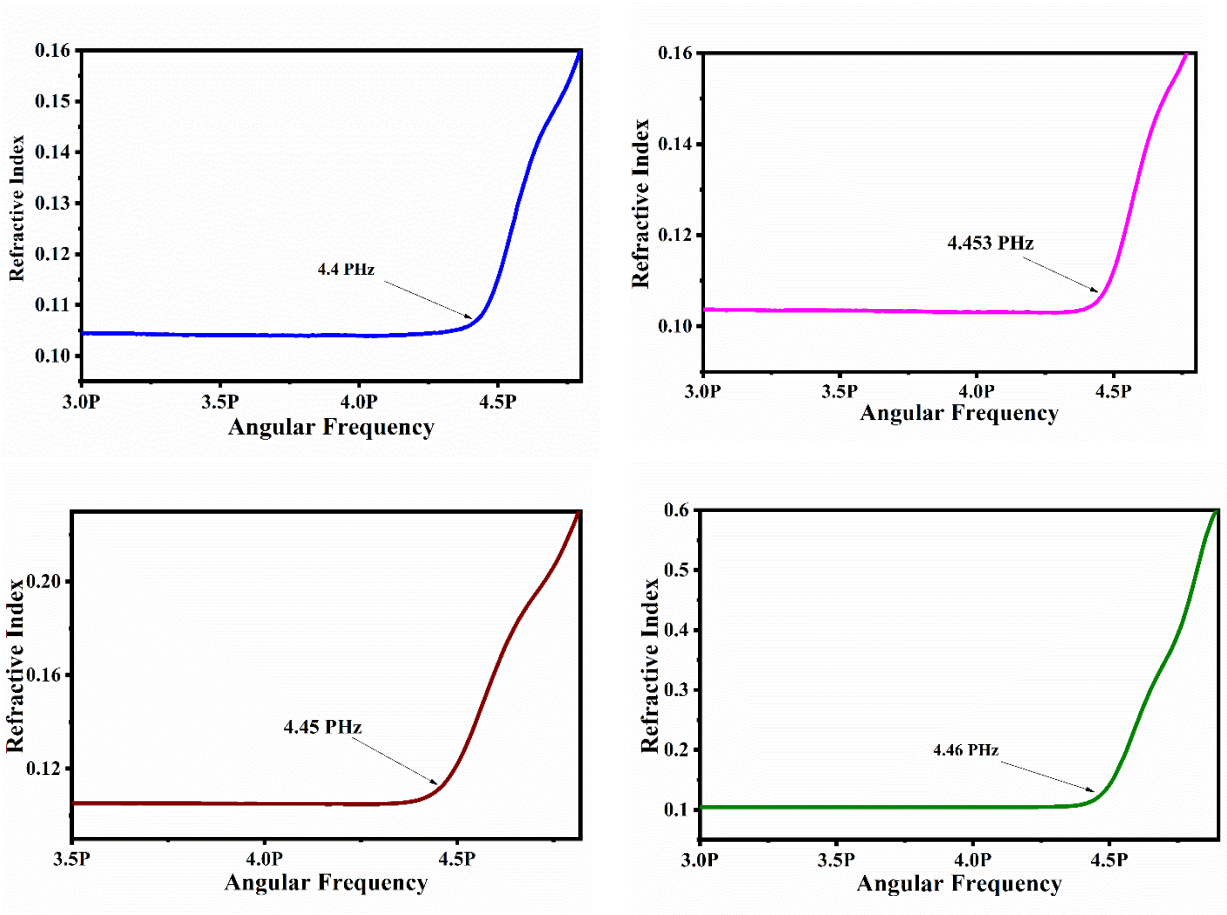

Figure 6. Normal dispersion region calculation and plot the angular frequency against refractive index of ADT molecule.

4.4Optical and electrical conductivity

The electrical and optical conductivity based on the following factors is two significant characteristics to depend on electrical and optical behaviors (Yoshino et al., 2008).

$$\sigma_{opt} = \frac{\alpha nc}{4\pi} \quad (11)$$

$$\sigma_{ele} = \frac{2\lambda\sigma_{opt}}{\alpha} \quad (12)$$

Regarding the electronic structure of materials, the electrical conductivity of materials and semiconductor optical conductivity is the differences in conductivity generated by irradiation, either a decrease or an increase. Drude model defined physical electrical conductivity, and the band theory is important in defining the idea of conductivity. When the valence and conduction bands intersect, the conduction band gains additional free electrons (Xie et al., 2018, Yang et al., 2013). The resistivity of the semiconductor material is described by the scattering phenomenon, and the electrons that are excited from the valence band to the conduction band are essential for conduction. In this mechanism, the dielectric constant of a material is connected to the ability of light to transport through the substance. The relaxation time and plasma frequency are crucial in optical propagation.

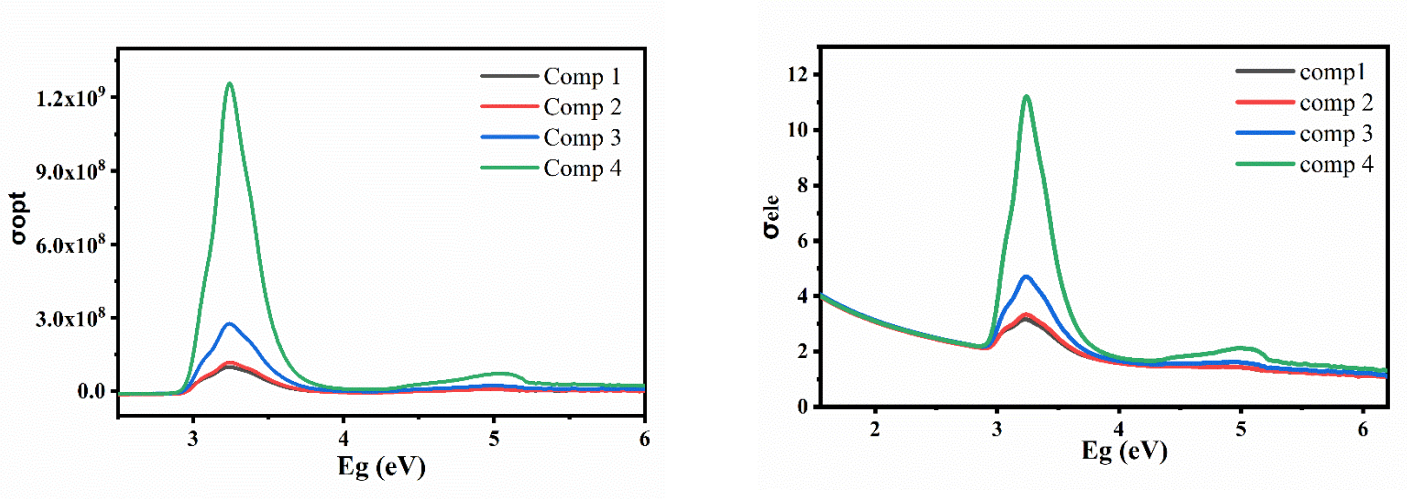

Figure 7. optical and electrical conductivity variation with a bandgap energy

The high conductivity may be optimized when photons have these peak energy levels. In this respect, band gap energy can be highly advantageous in terms of electrical transmission since the M4 molecule has a wide bandgap and rising optical conductance at 3 eV to 3.6 eV, which is particularly useful for the construction of materials operating at high temperatures and voltage, such as solar cells. The dielectric constant is an important quantity in the study of material conduction characteristics. The use of the film for photovoltaic applications is determined by the electrical characteristics of the materials, which are critical in deciding the application (Rayssi et al., 2018). The real component of the dielectric constant indicates the speed of light that can restrict the compound. The imaginary component of the dielectric constant depicts the absorption of light energy by an electric field owing to dipole motion. The process variables ε' and ε'' indicate the real component of the dielectric constant and the imaginary part (dielectric loss). The complex dielectric constant may be calculated using the following formula (Sassi et al., 2017):

$$\varepsilon^* = \varepsilon' + j\varepsilon'' \quad (13)$$

Material dielectric spectroscopy is critical due to being linked to many factors, such as grain with grain boundary and insights into the structure of compounds, transportation properties, and charge storage capacities of dielectric materials. Potential barrier gene rates in thin films or materials at grain boundaries produce a rise in dielectric constant with increasing frequency and are connected to the availability of space charge polarization (Xie et al., 2018, Yang et al., 2013). The difference between these materials is large in terms of dielectric constant, with the former having the highest amount in both the real and imaginary parts, shown in Figure 8.

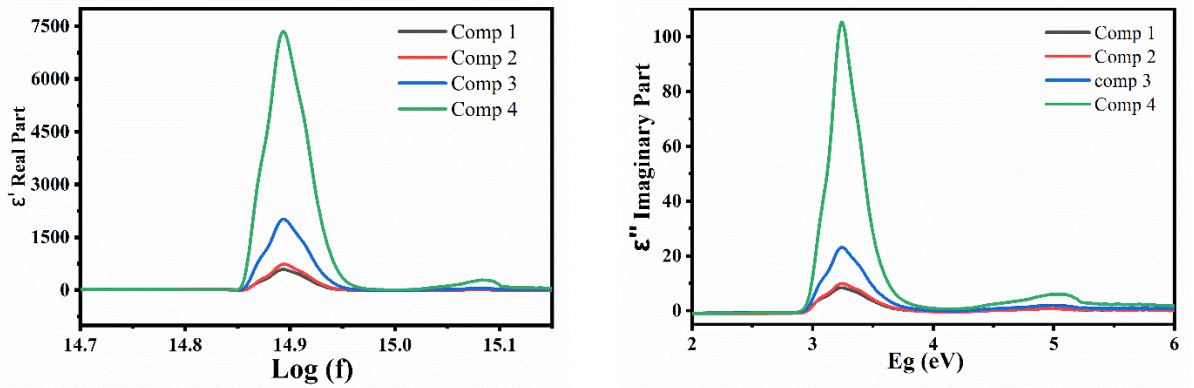

Figure 8. (A) real part of dielectric constant and frequency, (B) Imaginary part of dielectric constant with band energy.

5.Electronic structure

The density functional theory (DFT) has a large range of user research methods for predicting the chemical interactions of clusters, solids, and molecules. DFT has grown in popularity over the last several decades. Gaussian software was used for all estimations in this investigation. The hybrid exchange-correlation functional (B3LYP) was used to optimize the geometry of the title molecule using DFT and Becke's three parameters (MAMAND, 2019, Qadr and MAMAND). This work made use of the 6-311++ G (d,p) basis set. This basis set yields more precise outcomes when determining geometries and electrochemical properties for a broad range of organic molecules. Calculations have been conducted in the gas and aqueous phases to make a comparison of chemical reactivity and intermolecular forces. Because electrochemistry occurs in the aqueous phase, the effect of solvent should be considered in the calculations. To study solvent calculations, the self-consistent reaction field technique (SCRF) predicated on the polarizable continuum model (PCM) has been used (Qadr and Mamand, 2021). This method models water solvent as the continuum dielectric constant of 78.5 and characterizes the soft-sphere cavity in which the organic solvent is positioned as a confederation of a series of mutually reinforcing atomic spheres. Numerous kinds of investigations based on the PCM model and the accuracy and dependability of the PCM method for solvent impact analysis have been taken into account for investigations (Cammi and Mennucci, 1999). The electronic structure parameters which determined the HOMO, LUMO, Ionization energy, Electron Affinity, Energy gap, Hardness, Softness, Electronegativity, Chemical potential, Electrophilicity, Nucleophilicity, Back-donation, Electron transfer, Dipole moment, and Total energy T.E for all compound (M2-M5) was show in Table 1-4. The compounds with Higher EHOMO and lower energy bandgap it is more reactive.

Table 1. Quantum chemical parameters of Structure M2

Quantum chemical parameters	Gas phase		Aqueous phase	
	Non-protonated	Protonated	Non-protonated	Protonated
HOMO (eV)	-6.118	-8.448	-5.778	-5.671
LUMO (eV)	-1.623	-4.155	-1.604	-1.598
Ionization energy (eV)	6.118	8.448	5.778	5.671
Electron Affinity (eV)	1.623	4.155	1.604	1.598
Energy gap (eV)	4.495	4.293	4.174	4.073
Hardness (eV)	2.2475	2.1465	2.087	2.0365
Softness (eV)-1	0.222	0.233	0.240	0.246
Electronegativity (eV)	3.8705	6.3015	3.691	3.6345
Chemical potential (eV)	-3.8705	-6.3015	-3.691	-3.6345
Electrophilicity (eV)	3.333	9.250	3.264	3.243
Nucleophilicity (eV)-1	0.300	0.108	0.306	0.308
Back-donation (eV)	-0.562	-0.537	-0.522	-0.509
Electron transfer	1.722	2.936	1.769	1.785
Dipole moment	3.073	3.359	4.579	21.081
Total energy T.E (a.u)	-2138.518	-2137.936	-2138.556	-2138.022

Table 2. Quantum chemical parameters of Structure M3.

Quantum chemical parameters	Gas phase		Aqueous phase	
	Non-protonated	Protonated	Non-protonated	Protonated
HOMO (eV)	-5.686	-8.383	-5.834	-5.642
LUMO (eV)	-1.481	-4.085	-1.573	-1.617
Ionization energy (eV)	5.686	8.383	5.834	5.642
Electron Affinity (eV)	1.481	4.085	1.573	1.617
Energy gap (eV)	4.205	4.298	4.261	4.025
Hardness (eV)	2.1025	2.149	2.1305	2.0125
Softness (eV)-1	0.238	0.233	0.235	0.248
Electronegativity (eV)	3.5835	6.234	3.7035	3.6295
Chemical potential (eV)	-3.5835	-6.234	-3.7035	-3.6295
Electrophilicity (eV)	3.054	9.042	3.219	3.273
Nucleophilicity (eV)-1	0.327	0.111	0.311	0.306
Back-donation (eV)	-0.526	-0.537	-0.533	-0.503
Electron transfer	1.704	2.901	1.738	1.803
Dipole moment	3.820	4.251	4.584	18.238
Total energy T.E (Hartree)	-2295.449	-2295.209	-2295.449	-2295.288

Table 3. Quantum chemical parameters of Structure M4

Quantum chemical parameters	Gas phase		Aqueous phase	
	Non-protonated	Protonated	Non-protonated	Protonated
HOMO (eV)	-5.678	-8.342	-5.997	-6.249
LUMO (eV)	-1.504	-4.048	-1.686	-1.866
Ionization energy (eV)	5.678	8.342	5.997	6.249
Electron Affinity (eV)	1.504	4.048	1.686	1.866
Energy gap (eV)	4.174	4.294	4.311	4.383
Hardness (eV)	2.087	2.147	2.1555	2.1915
Softness (eV)-1	0.240	0.233	0.232	0.228
Electronegativity (eV)	3.591	6.195	3.8415	4.0575
Chemical potential (eV)	-3.591	-6.195	-3.8415	-4.0575
Electrophilicity (eV)	3.089	8.938	3.423	3.756
Nucleophilicity (eV)-1	0.324	0.112	0.292	0.266
Back-donation (eV)	-0.522	-0.537	-0.539	-0.548
Electron transfer	1.721	2.885	1.782	1.851
Dipole moment (Debye)	3.696	4.189	4.644	20.332
Total energy T.E (Hartree)	-2452.653	-2452.413	-2452.667	-2452.467

Table 4. Quantum chemical parameters of Structure M5.

Quantum chemical parameters	Gas phase		Aqueous phase	
	Non-protonated	Protonated	Non-protonated	Protonated
HOMO (eV)	-5.684	-8.454	-5.934	-6.411
LUMO (eV)	-1.483	-4.241	-1.637	-1.923
Ionization energy (eV)	5.684	8.454	5.934	6.411
Electron Affinity (eV)	1.483	4.241	1.637	1.923
Energy gap (eV)	4.201	4.213	4.297	4.488
Hardness (eV)	2.1005	2.1065	2.1485	2.244
Softness (eV)-1	0.238	0.237	0.233	0.223
Electronegativity (eV)	3.5835	6.3475	3.7855	4.167
Chemical potential (eV)	-3.5835	-6.3475	-3.7855	-4.167
Electrophilicity (eV)	3.057	9.563	3.335	3.869
Nucleophilicity (eV)-1	0.327	0.105	0.300	0.258
Back-donation (eV)	-0.525	-0.527	-0.537	-0.561
Electron transfer	1.706	3.013	1.762	1.857
Dipole moment	3.938	4.173	4.015	11.774
Total energy T.E (Hartree)	-2609.981	-2609.110	-2609.981	-2609.197

E_{HOMO} is associated with a molecule's capability to donate electrons. Multiple studies have shown that inhibitors with high E_{HOMO} values are inclined to donate electrons to a suitable acceptor with a low empty molecular orbital energy (Erdoğan et al., 2017). The capacity of compounds to accept electrons is determined by E_{LUMO}. A higher E_{LUMO} result represents that the compound is less likely to accept electrons. For example, the compounds can accept an electron from the d orbital but also donate an electron from the d orbital to the unoccupied d orbital of the metal surface, leading to the development of a response bond. See Figure **9** Ranking of EHOMO and ELUMO of selected molecules basis on DFT calculation in protonated and non-protonated species at gas and aqueous phase.

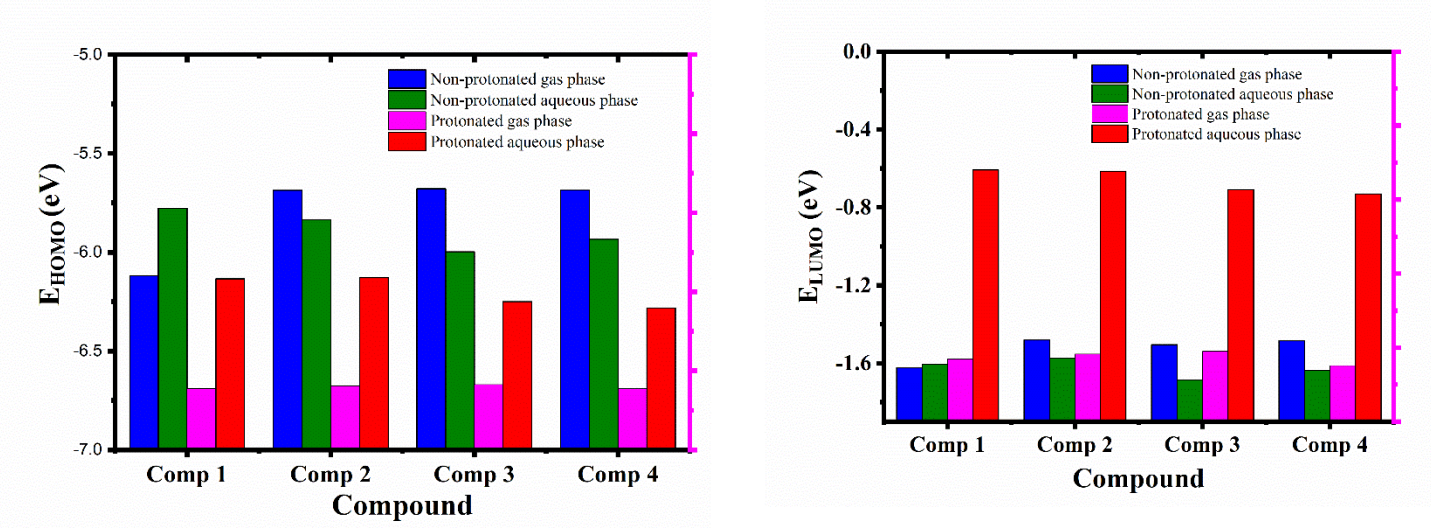

Figure 9. Ranking of EHOMO and ELUMO of selected molecules basis on DFT calculation in protonated and non-protonated species at gas and aqueous phase.

In non-protonated species, the M2 molecule has the highest value of E_{HOMO} in the aqueous phase, but in non-protonated gas, the M3 molecule has the highest value of E_{HOMO}, as shown in Figure 9,

this shows that it can donate electrons. In contrast, in the protonated aqueous phase, the highest values were observed for all molecules, with the first compound having the highest in terms of E_{LUMO}, in which case all molecules have specifically much higher electron uptake capacity. The compounds used in this study vary in quantum chemical properties according to different phases and states. The bandgap energy of the compounds determined the degree of reactivity, and a wide bandgap corresponds to the unreactive compounds (Mamand and Qadr, 2022). Due to the effect of small and high bandgaps on compound reactivity, the energy gap is a crucial characteristic as a measure of the inhibitor molecule's reactivity towards adsorption on the material surface (Chattaraj and Roy, 2007).

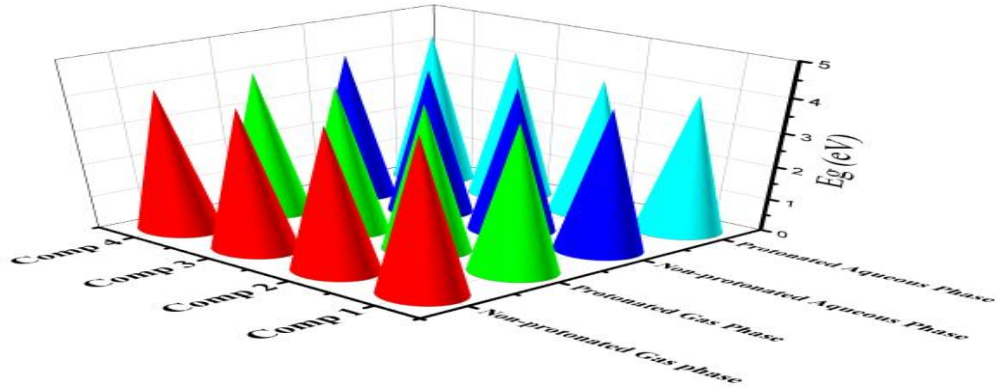

Figure 10. Energy gap order of all compounds in gas and aqueous phase at protonated and non-protonated species.

The M3 and M2 molecules in the gas phase at protonated species in the aqueous phase have the smallest bandgap energy, while the M5 compound in the protonated aqueous phase, the M2 compound in the non-protonated gas phase, and the M4 compound non-protonated aqueous phase have the highest bandgap energy, as shown in Figure 10. The physical and chemical properties of drugs in the aqueous phase are very sensitive because water negatively affects the physical and chemical stability of a drug substance. In this study, in water phase calculated the physicochemical properties because water plays an important role, no matter where it is present, in the active ingredient, excipients, or the atmosphere. Water can affect many chemical behaviors of drugs such as may lead to phase shifts, dissolution of soluble components, and increased interactions between drugs and excipients.

To make sure the findings of the computation are correct, the hardness and softness of the molecule must be calculated. The hardness characteristic associated with the electron clouds of molecules, atoms, and ions primarily reflects the resistance to deformation or polarization of the electron cloud of the atoms, ions, or molecules during minor chemical process disruption (Obot and Obi-Egbedi, 2010). The compounds with the highest global softness and lowest hardness are likely to be powerful corrosion inhibitors for bulk materials in acidic environments. If the molecule has a reduced hardness and a higher smoothness, it suggests that the inhibitor is adsorbing on a metal surface in a portion of the compound (Qiang et al., 2017). In this study, the sequence of the softness of compounds is shown in Table 5. Softness may be used to characterize and quantify the chemical response of pharmacological molecules. The highest site of the compound has a high rate of reaction, and the reaction happens relatively readily in the region of the molecule with the highest softness. The number of electrons transported to the molecules beneath the probe was determined using DFT for each protonated and non-protonated state in the gas phase and aqueous phase, as shown in Tables 1-4. If $\Delta N > 3.6$, the inhibitory efficiency rose as the metal surface's electron-donating capacity grew (De Proft and Geerlings, 2001). The highest values were observed in the unprotonated gas and protonated aqueous phase, suggesting that in these two cases, the ability to donate electrons is high, and in other cases, the molecules have a higher tendency to give electrons (Lukovits et al., 2001).

Table 5. the Ranking of the softness of selected molecules

Non-protonated Gas Phase	Protonated Gas Phase	Non-protonated Aqueous Phase	Protonated Aqueous Phase
1>4>2>3	1>2>3>4	3>4>2>1	4>3>2>1

6.Electrostatic potential map

To explore the deep electron structure, (Leboeuf et al., 1997). (Ramalingam et al., 2011). .

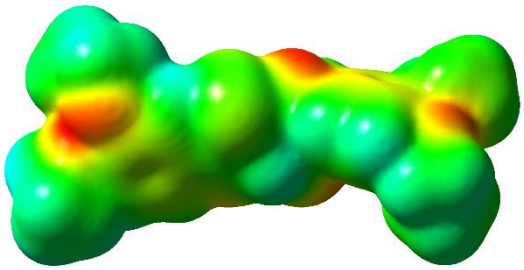

MEP M2

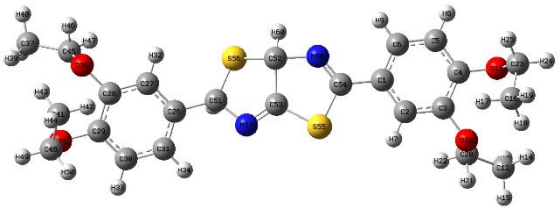

Structure M2

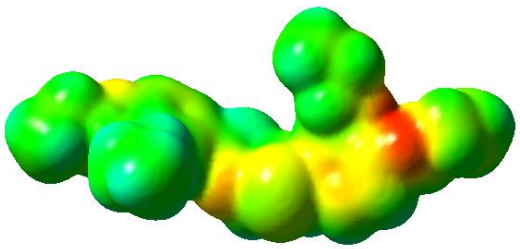

MEP M3

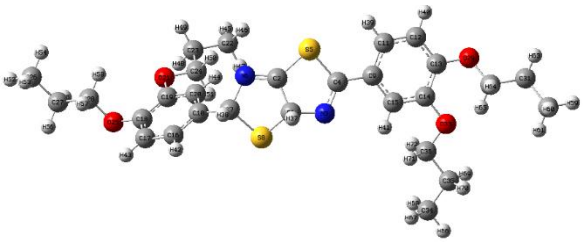

Structure M3

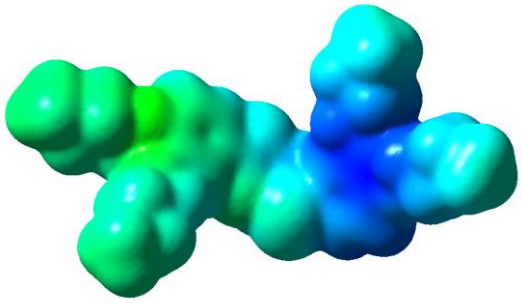

MEP M4

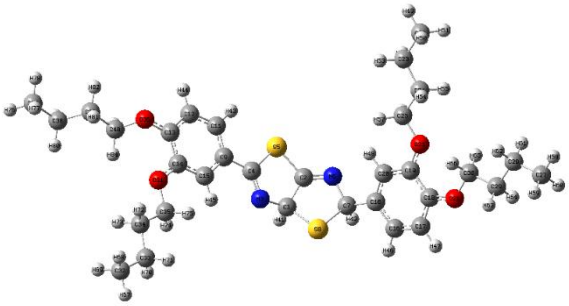

Structure M4

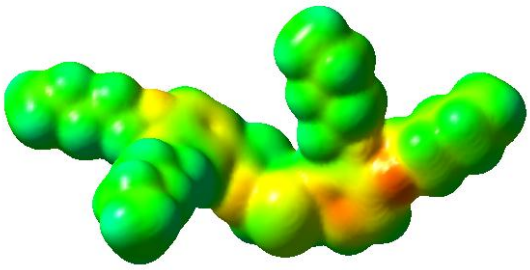

MEP M5

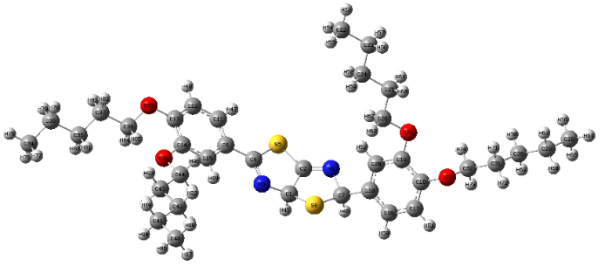

Structure M5

Figure 11. MEP and Optimized structure for all structures

7.Thermodynamic parameters

The important thermodynamic parameters, such as enthalpy (H), entropy (S), free energy (G), and heat capacity (Cv), were calculated for the title compounds when they were using DFT with the 6-311++G (d, p) basis set in the gas phase at temperatures between 100 and 1000 Kelvin. These results are presented in Figure 12. The thermal parameters were calculated using gaussian software. In addition, the thermodynamical parameters are used to describe the state as well as direction of a chemical reaction. Furthermore, these parameters also examine the spontaneity of a reaction, its energy profile, that is, either endothermic or exothermic, and describe temperature effects on different thermodynamic properties. It was observed that entropy, heat capacity, and enthalpy increase as temperature rises (Akinbulumo et al., 2020, Al-Doori and Shihab, 2014). Whereas, free energy decreases with increasing temperatures. .

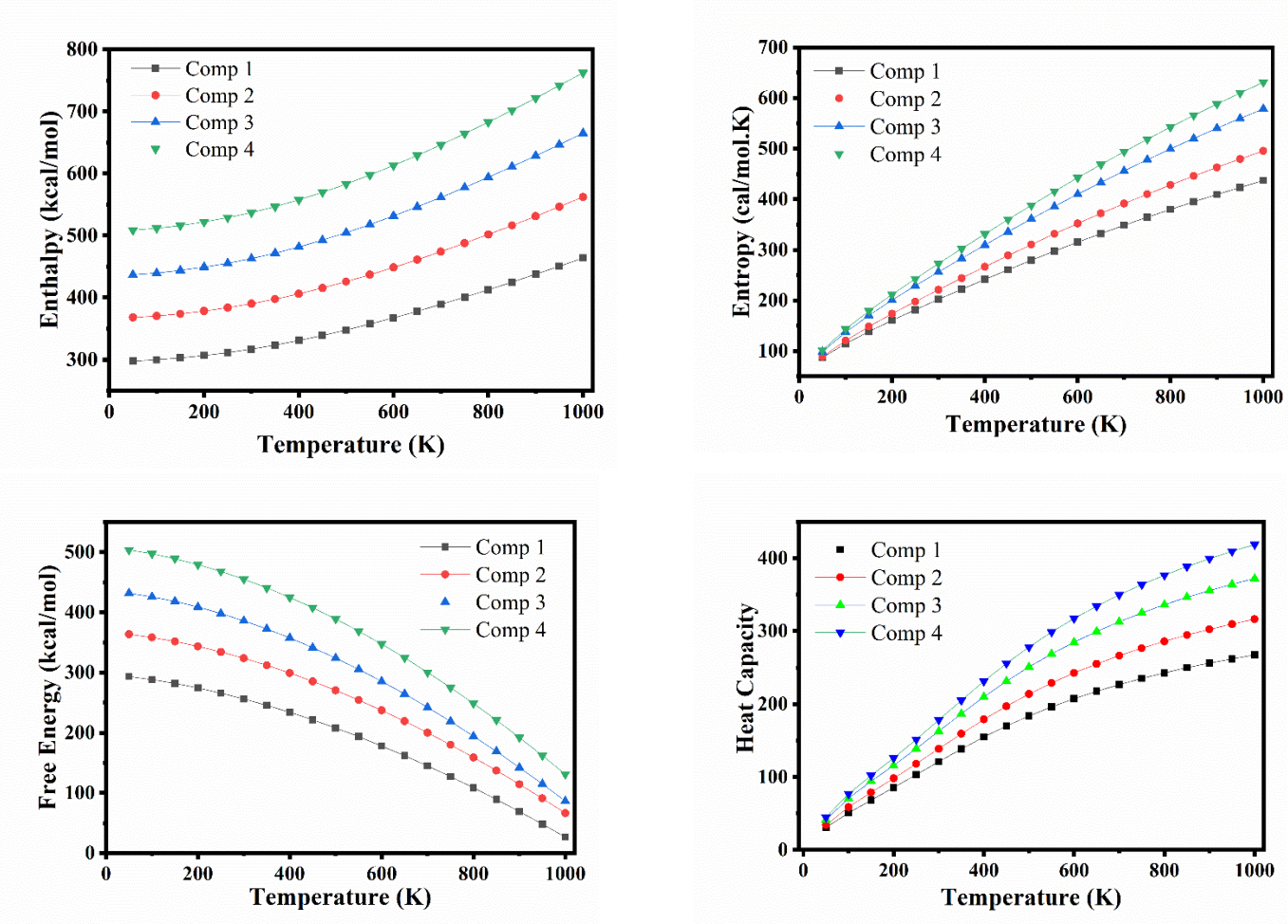

Figure 12. Thermodynamic

8.Molecular dynamic simulation

[36] are a useful and modern tool for exploring how inhibitors interact with metal surfaces, and can be implemented to do so. Molecular dynamics simulation investigations have been carried out to establish the binding energies of these molecules on the iron surface and if there is a significant association between experimental inhibition performances and binding energies for the molecules included in this work. Table 6 shows the calculated energies for total adsorption, stiff adsorption, and deformation and shows that extraordinarily high binding energies were calculated for interactions between inhibitors and metallic alloys (Erdoğan et al., 2017, Ghanbari et al., 2010, Raicheva et al., 1993).. It is critical to note that greater binding energy leads in a stronger inhibitor/surface interaction. Chemisorption has substantially greater adsorption energy than physical adsorption. As a result, such a link will

last longer at greater temperatures. Energy is reported to be released during the adsorption process by solubilized adsorption components deposited on the substrate see Figure 13. Adsorption energy is created by increasing the solid's adsorption energy and deforming the adsorption structure. A larger negative adsorption energy value indicates a stronger and more stable interaction between a metal and the molecule.

Table 6. The outputs and descriptors calculated by the Monte Carlo simulation for adsorption of selected inhibitors on Fe (110) (in kcal mol^{-1}) and experimental inhibition efficiency.

Compounds	Total energy	Adsorption energy	Rigid adsorption	Deformation energy	dE_{ad}/dN_i
M2	70.85072264	-337.47201463	-7.69844723	-329.77356740	-337.47201463
M3	76.87001901	-1.782107e+015	-8.36439320	-1.782107e+015	-1.782107e+015
M4	95.27913475	-3.428051e+007	-7.37964460	-3.428050e+007	-3.428051e+007
M5	90.33208457	-1.692075e+005	-12.03512532	-1.691955e+005	-1.692075e+005

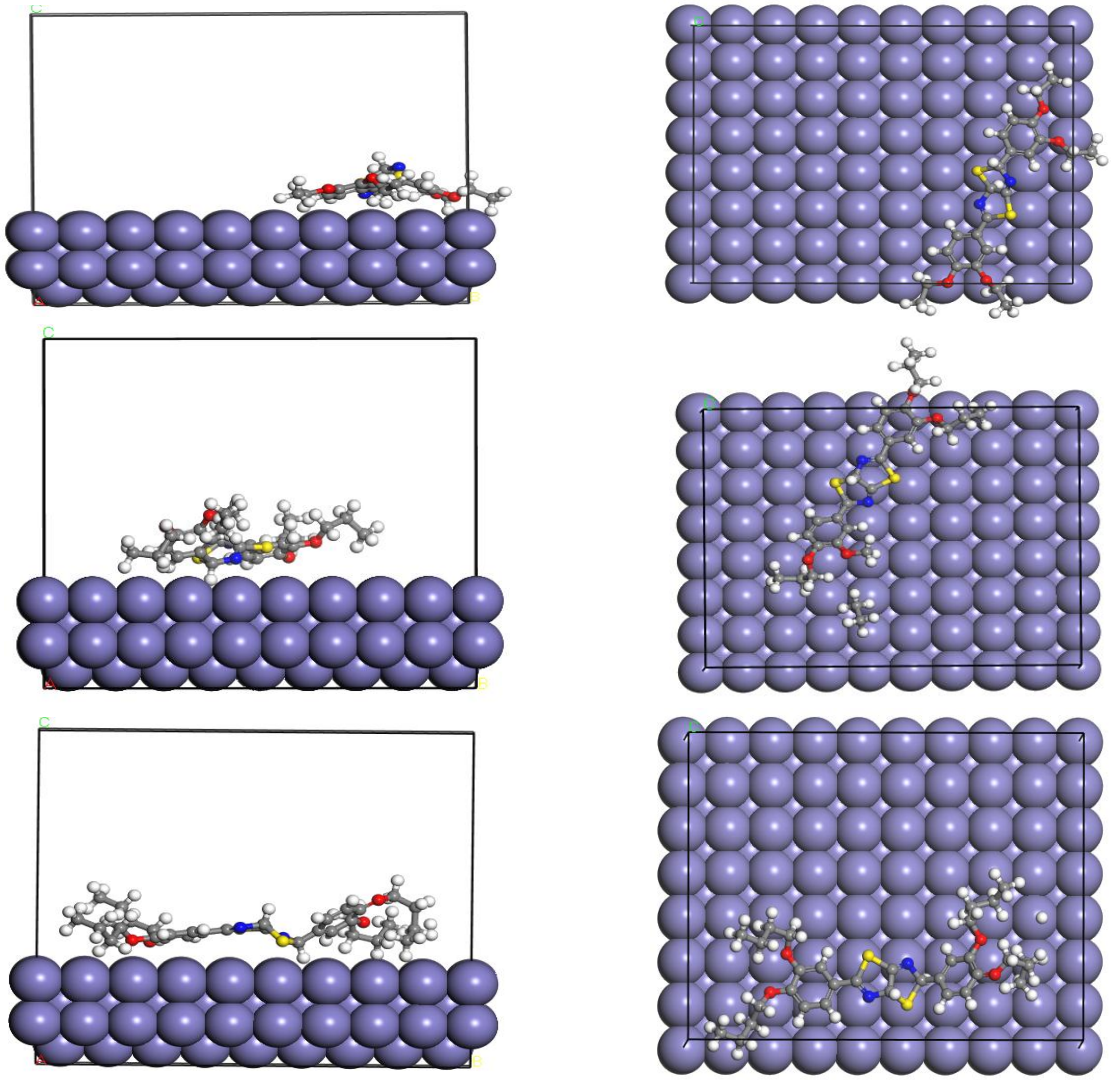

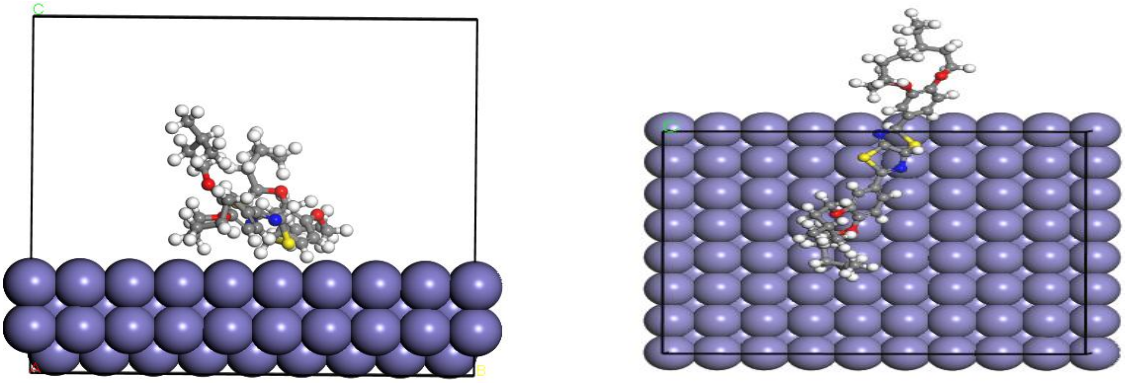

Figure 13. Top view and side view of monte carlo simulation at most stable low energy configuration for adsorption on Fe (110) surface

9.Conclusion

UV-visible spectroscopy is a powerful tool for analyzing materials, particularly for determining the size, concentration, and bandgap energy of nanoparticles. It can also be used to measure the absorption coefficient, transmittance, and electrical conductivity of materials. Furthermore, the Tauc plot is a useful tool for determining the bandgap energy associated with the highest

absorption of light peaks. The refractive index, bandgap energy, and complex dielectric constant are essential to determine the electrical and optical characteristics of materials. The ADT molecule has a wide bandgap and a high optical conductivity, making it suitable for use in the construction of high-temperature and voltage materials, such as solar cells. This investigation has demonstrated that the EHOMO and ELUMO values of the compounds vary according to different phases and states. The hardness and softness of the compounds have also been calculated, with those with the highest global softness and lowest hardness being the most powerful corrosion inhibitors for bulk materials in acidic environments.

The thermodynamic parameters of enthalpy, entropy, free energy, and heat capacity were observed to increase with increasing temperatures, except for free energy. Molecular dynamics simulations have also been used to examine the interaction of inhibitors with metal surfaces, and it was found that greater binding energy leads to a stronger inhibitor/surface interaction. The adsorption energy is created by increasing the solid's adsorption energy and deforming the adsorption structure and a larger negative adsorption energy value indicates a stronger and more stable interaction between a metal and the molecule.

References

ACHAR, B. & LOKESH, K. 2004. Studies on phthalocyanine sheet polymers. *Journal of organometallic chemistry,* 689**,** 2601-2605.

AKINBULUMO, O. A., ODEJOBI, O. J. & ODEKANLE, E. L. 2020. Thermodynamics and adsorption study of the corrosion inhibition of mild steel by Euphorbia heterophylla L. extract in 1.5 M HCl. *Results in Materials,* 5**,** 100074.

AKL, A. A. 2004. Optical properties of crystalline and non-crystalline iron oxide thin films deposited by spray pyrolysis. *Applied Surface Science,* 233**,** 307-319.

AL-DOORI, H. H. & SHIHAB, M. S. 2014. Study of Some [N-substituted] p-aminoazobenzene as Corrosion Inhibitors for Mild-Steel in 1M H2SO4. *Al-Nahrain Journal of Science,* 17**,** 59-68.

AL-KUHAILI, M., SALEEM, M. & DURRANI, S. 2012. Optical properties of iron oxide (α-Fe2O3) thin films deposited by the reactive evaporation of iron. *Journal of alloys and compounds,* 521**,** 178-182.

AYDIN, H., GÜNDÜZ, B. & AYDIN, C. 2019. Surface morphology, spectroscopy, optical and conductivity properties of transparent poly (9-vinylcarbazole) thin films modified with graphene oxide. *Synthetic Metals,* 252**,** 1-7.

BOHREN, C. F. & HUFFMAN, D. R. 2008. *Absorption and scattering of light by small particles,* John Wiley & Sons.

BUKOWCZAN, A., HEBDA, E. & PIELICHOWSKI, K. 2021. The influence of nanoparticles on phase formation and stability of liquid crystals and liquid crystalline polymers. *Journal of Molecular Liquids,* 321**,** 114849.

CAMMI, R. & MENNUCCI, B. 1999. Linear response theory for the polarizable continuum model. *The Journal of chemical physics,* 110**,** 9877-9886.

CHATTARAJ, P. K. & ROY, D. R. 2007. Update 1 of: electrophilicity index. *Chemical reviews,* 107**,** PR46-PR74.

CHRISTOFFERSEN, E., STOLTZE, P. & NØRSKOV, J. K. 2002. Monte Carlo simulations of adsorption-induced segregation. *Surface science,* 505**,** 200-214.

DE PROFT, F. & GEERLINGS, P. 2001. Conceptual and computational DFT in the study of aromaticity. *Chemical reviews,* 101**,** 1451-1464.

EPSTEIN, R., SHEIK-BAHAE, M. & HEHLEN, M. 2009. Optical Refrigeration. *Science and Applications of Laser Cooling of Solids., Wiley*.

ERDOĞAN, Ş., SAFI, Z. S., KAYA, S., IŞıN, D. Ö., GUO, L. & KAYA, C. 2017. A computational study on corrosion inhibition performances of novel quinoline derivatives against the corrosion of iron. *Journal of Molecular Structure,* 1134**,** 751-761.

GALLARDO, H., MAGNAGO, R. & BORTOLUZZI, A. J. 2001. Synthesis, characterization and mesomorphic properties of Ag (I) and Pd (II) complexes containing the pyridyl and tetrazoyl rings: crystal structure of [C30H46N10Ag ClO4]. *Liquid Crystals,* 28**,** 1343-1352.

GHANBARI, A., ATTAR, M. & MAHDAVIAN, M. 2010. Corrosion inhibition performance of three imidazole derivatives on mild steel in 1 M phosphoric acid. *Materials Chemistry and Physics,* 124**,** 1205-1209.

GUO, L., ZHU, S. & ZHANG, S. 2015. Experimental and theoretical studies of benzalkonium chloride as an inhibitor for carbon steel corrosion in sulfuric acid. *Journal of Industrial and Engineering Chemistry,* 24**,** 174-180.

HA, S.-T., KOH, T.-M., LIN, H.-C., YEAP, G.-Y., WIN, Y.-F., ONG, S.-T., SIVASOTHY, Y. & ONG, L.-K. 2009. Heterocyclic benzothiazole-based liquid crystals: synthesis and mesomorphic properties. *Liquid Crystals,* 36**,** 917-925.

HAMAD, W. M., AZIZ, H. J. & AL-DUJAILI, A. H. Synthesis and liquid crystalline studies of some heterocyclic compounds with lateral long chain substituents, 2004.

HAN, J., CHANG, X. Y., ZHU, L. R., WANG, Y. M., MENG, J. B., LAI, S. W. & CHUI, S. S. Y. 2008. Synthesis and liquid crystal properties of a new class of calamitic mesogens based on substituted 2, 5-diaryl-1, 3, 4-thiadiazole derivatives with wide mesomorphic temperature ranges. *Liquid Crystals,* 35**,** 1379-1394.

KOPARIR, P., OMAR, R. A., SARAC, K., AHMED, L. O., KARATEPE, A., TASKIN-TOK, T. & SAFIN, D. A. 2022. Synthesis, Characterization and Computational Analysis of Thiophene-2, 5-Diylbis ((3-Mesityl-3-Methylcyclobutyl) Methanone). *Polycyclic Aromatic Compounds***,** 1-19.

LEBOEUF, M., KÖSTER, A. & SALAHUB, D. 1997. Approximation of the molecular electrostatic potential in a gaussian density functional method. *Theoretical Chemistry Accounts,* 96**,** 23-30.

LI, Y., CONCELLÓN, A., LIN, C.-J., ROMERO, N. A., LIN, S. & SWAGER, T. M. 2020. Thiophene-fused polyaromatics: synthesis, columnar liquid crystal, fluorescence and electrochemical properties. *Chemical Science,* 11**,** 4695-4701.

LUKOVITS, I., KALMAN, E. & ZUCCHI, F. 2001. Corrosion inhibitors—correlation between electronic structure and efficiency. *Corrosion,* 57**,** 3-8.

MAMAND, D. 2019. Theoretical calculations and spectroscopic analysis of gaussian computational examination-NMR, FTIR, UV-Visible, MEP on 2, 4, 6-Nitrophenol. *Journal of Physical Chemistry and Functional Materials,* 2**,** 77-86.

MAMAND, D. M. & QADR, H. M. 2021. Comprehensive spectroscopic and optoelectronic properties of bbl organic semiconductor. *Protection of Metals and Physical Chemistry of Surfaces,* 57**,** 943-953.

MAMAND, D. M. & QADR, H. M. 2022. Density Functional Theory and Computational Simulation of the Molecular Structure on Corrosion of Carbon Steel in Acidic Media of Some Amino Acids. *Russian Journal of Physical Chemistry A,* 96**,** 2155-2165.

MAMAND, D. M., RASUL, H. H., OMER, P. K. & QADR, H. M. 2022. Theoretical and experimental investigation on ADT organic semiconductor in different solvents. *Condensed Matter and Interphases,* 24**,** 227-242.

MATHARU, A. & CHAMBERS-ASMAN, D. 2007. Structure–property investigation of 2-and 3-thienylacrylates bearing laterally fluorinated azobenzene moieties. *Liquid Crystals,* 34**,** 1317-1336.

MAURYA, A. & AWASTHI, D. K. 2022. An Introduction to Liquid Crystals and It's Types Nematic, Smetic and Cholestric Crystals. *International Research Journal of Innovations in Engineering and Technology,* 6**,** 101.

NAFEE, S. S., AHMED, H. & HAGAR, M. 2020. Theoretical, experimental and optical study of new thiophene-based liquid crystals and their positional isomers. *Liquid Crystals,* 47**,** 1291-1302.

OBOT, I. & OBI-EGBEDI, N. 2010. Adsorption properties and inhibition of mild steel corrosion in sulphuric acid solution by ketoconazole: experimental and theoretical investigation. *Corrosion Science,* 52**,** 198-204.

OMER, R., KOPARIR, P., KOPARIR, M., RASHID, R., AHMED, L. & HAMA, J. 2022a. Synthesis, Characterization and DFT Study of 1-(3-Mesityl-3-methylcyclobutyl)-2-((4-phenyl-5-(thiophen-2-yl)-4H-1, 2, 4-triazol-3-yl) thio) ethan-1-one. *Protection of Metals and Physical Chemistry of Surfaces***,** 1-13.

OMER, R. A., KOPARIR, P. & AHMED, L. 2022b. Theoretical determination of corrosion inhibitor activities of 4-allyl-5-(pyridin-4-yl)-4H-1, 2, 4-triazole-3-thiol-thione tautomerism. *Indian Journal of Chemical Technology (IJCT),* 29**,** 75-81.

OMER, R. A., KOPARIR, P. & AHMED, L. O. 2022c. Characterization and inhibitor activity of two newly synthesized thiazole. *Journal of Bio-and Tribo-Corrosion,* 8**,** 28.

ONG, L.-K., HA, S.-T., YEAP, G.-Y. & LIN, H.-C. 2018. Heterocyclic pyridine-based liquid crystals: synthesis and mesomorphic properties. *Liquid Crystals,* 45**,** 1574-1584.

OREK, C., GÜNDÜZ, B., KAYGILI, O. & BULUT, N. 2017. Electronic, optical, and spectroscopic analysis of TBADN organic semiconductor: Experiment and theory. *Chemical Physics Letters,* 678**,** 130-138.

OU, Z., SHEN, J. & KADISH, K. M. 2006. Electrochemistry of Aluminum Phthalocyanine: Solvent and Anion Effects on UV− Visible Spectra and Reduction Mechanisms. *Inorganic chemistry,* 45**,** 9569-9579.

PARLAK, A. E., OMAR, R. A., KOPARIR, P. & SALIH, M. I. 2022. Experimental, DFT and Theoretical Corrosion Study for 4-(((4-ethyl-5-(thiophen-2-yl)-4H-1, 2, 4-triazole-3-yl) thio) methyl)-7, 8-dimethyl-2H-chromen-2-one. *Arabian Journal of Chemistry,* 15**,** 104088.

PARRA, M., ELGUETA, E., ULLOA, J., VERGARA, J. & SANCHEZ, A. 2012. Columnar liquid crystals based on amino-1, 3, 4-thiadiazole derivatives. *Liquid Crystals,* 39**,** 917-925.

PETROV, V., PAVLUCHENKO, A. & SMIRNOVA, N. 1995. New liquid crystalline pyridine derivatives. *Molecular Crystals and Liquid Crystals Science and Technology. Section A. Molecular Crystals and Liquid Crystals,* 265**,** 47-53.

PLATSCHEK, B. 2007. *Ordered Mesoporous Silica: Control of Morphology and Exploration with Single Molecules.* lmu.

QADR, H. M. & MAMAND, D. Monte Carlo calculation of absorbed dose under MeV proton irradiation. *Journal of Physical Chemistry and Functional Materials,* 5**,** 7-11.

QADR, H. M. & MAMAND, D. M. 2021. Molecular structure and density functional theory investigation corrosion inhibitors of some oxadiazoles. *Journal of Bio-and Tribo-Corrosion,* 7**,** 140.

QIANG, Y., ZHANG, S., GUO, L., ZHENG, X., XIANG, B. & CHEN, S. 2017. Experimental and theoretical studies of four allyl imidazolium-based ionic liquids as green inhibitors for copper corrosion in sulfuric acid. *Corrosion Science,* 119**,** 68-78.

RAICHEVA, S., ALEKSIEV, B. & SOKOLOVA, E. 1993. The effect of the chemical structure of some nitrogen-and sulphur-containing organic compounds on their corrosion inhibiting action. *Corrosion Science,* 34**,** 343-350.

RAMALINGAM, S., BABU, P. D. S., PERIANDY, S. & FEREYDUNI, E. 2011. Vibrational investigation, molecular orbital studies and molecular electrostatic potential map analysis on 3-chlorobenzoic acid using hybrid computational calculations. *Spectrochimica Acta Part A: Molecular and Biomolecular Spectroscopy,* 84**,** 210-220.

RAVINDRA, N., GANAPATHY, P. & CHOI, J. 2007. Energy gap–refractive index relations in semiconductors–An overview. *Infrared physics & technology,* 50**,** 21-29.

RAYSSI, C., KOSSI, S. E., DHAHRI, J. & KHIROUNI, K. 2018. Frequency and temperature-dependence of dielectric permittivity and electric modulus studies of the solid solution Ca 0.85 Er 0.1 Ti 1− x Co 4x/3 O 3 (0≤ x≤ 0.1). *Rsc Advances,* 8**,** 17139-17150.

REBAZ, O., KOPARIR, P., QADER, I. & AHMED, L. 2022. Theoretical Determination of Corrosion Inhibitor Activities of Naphthalene and Tetralin. *Gazi University Journal of Science***,** 1-1.

SASSI, M., OUESLATI, A., MOUTIA, N., KHIROUNI, K. & GARGOURI, M. 2017. A study of optical absorption and dielectric properties in lithium chromium diphosphate compound. *Ionics,* 23**,** 847-855.

SEED, A. 2007. Synthesis of self-organizing mesogenic materials containing a sulfur-based five-membered heterocyclic core. *Chemical Society Reviews,* 36**,** 2046-2069.

SHAHBAZI, H., TATAEI, M., ENAYATI, M., SHAFEIEY, A. & MALEKABADI, M. A. 2019. Structure-transmittance relationship in transparent ceramics. *Journal of Alloys and Compounds,* 785**,** 260-285.

SHAN, H., ZHANG, H., LIU, J., WANG, S., MA, X., ZHANG, L., LIU, D., XIE, C. & TAO, Z. Retrieval method of aerosol extinction coefficient profile by an integral lidar system and case study. Fourth Seminar on Novel Optoelectronic Detection Technology and Application, 2018. International Society for Optics and Photonics, 106971D.

SHARMA, V. S., SHAH, A. P. & SHARMA, A. S. 2019. A new class of supramolecular liquid crystals derived from azo calix [4] arene functionalized 1, 3, 4-thiadiazole derivatives. *New Journal of Chemistry,* 43**,** 3556-3564.

SINGH, S. 2000. Phase transitions in liquid crystals. *Physics Reports,* 324**,** 107-269.

TEOH, W.-J., TUN NUR ISKANDAR, N. A. J., YEAP, G.-Y., KANEKO, K., SHIMIZU, A. & ITO, M. M. 2022. Experimental and computational studies of laterally ethoxy Schiff base-ester liquid crystalline magnets. *Liquid Crystals,* 49**,** 875-885.

TODORAN, D., TODORAN, R., SZAKÁCS, Z. & ANITAS, E. 2018. Electrical conductivity and optical properties of pulsed laser deposited LaNi5 nanoscale films. *Materials,* 11**,** 1475.

TOFT, J. & KVALHEIM, O. M. 1993. Eigenstructure tracking analysis for revealing noise pattern and local rank in instrumental profiles: application to transmittance and absorbance IR spectroscopy. *Chemometrics and intelligent laboratory systems,* 19**,** 65-73.

TOMI, I. H. R., AL-KARAWI, A. J. M., OMARALI, A.-A. B. & AL-HEETIMI, D. T. 2021. Liquid crystal behavior of Ag (I) complexes based on a series of mesogenic 1, 3, 4-thiadiazole ligands. *Molecular Crystals and Liquid Crystals,* 722**,** 8-26.

TRIPATHY, S. 2015. Refractive indices of semiconductors from energy gaps. *Optical materials,* 46**,** 240-246.

TURAN, N., KAYA, E., GÜNDÜZ, B., ÇOLAK, N. & KÖRKOCA, H. 2012. Synthesis, characterization of poly (E)-3-amino-4-((3-bromophenyl) diazenyl)-1H-pyrazol-5-ol: Investigation of antibacterial activity, fluorescence, and optical properties. *Fibers and Polymers,* 13**,** 415-424.

VARDAR, D., AKDAŞ KıLıÇ, H., OCAK, H., JEANNIN, O., CAMEREL, F. & ERAN, B. B. 2021. Pyridine-based chiral smectogens: effects of polar end groups on liquid crystal properties. *Liquid Crystals,* 48**,** 616-625.

WU, L.-H., WANG, Y.-C. & HSU, C.-S. 2000. Synthesis and characterization of thiophene-containing liquid crystals. *Liquid Crystals,* 27**,** 1503-1513.

XIE, P., WANG, Z., ZHANG, Z., FAN, R., CHENG, C., LIU, H., LIU, Y., LI, T., YAN, C. & WANG, N. 2018. Silica microsphere templated self-assembly of a three-dimensional carbon network with stable radio-frequency negative permittivity and low

dielectric loss. *Journal of Materials Chemistry C*, 6**,** 5239-5249.

YANG, K., HUANG, X., HUANG, Y., XIE, L. & JIANG, P. 2013. Fluoro-polymer@ BaTiO3 hybrid nanoparticles prepared via RAFT polymerization: toward ferroelectric polymer nanocomposites with high dielectric constant and low dielectric loss for energy storage application. *Chemistry of Materials*, 25**,** 2327-2338.

YEAP, G. Y., HA, S. T., LIM, P. L., BOEY, P. L., ITO, M. M., SANEHISA, S. & YOUHEI, Y. 2006. Synthesis, physical and mesomorphic properties of Schiff's base esters containing ortho-, meta-and para-substituents in benzylidene-4′-alkanoyloxyanilines. *Liquid crystals*, 33**,** 205-211.

YEAP*, G.-Y., HA, S.-T., LIM, P.-L., BOEY, P.-L., MAHMOOD, W. A. K., ITO, M. M. & SANEHISA, S. 2004. Synthesis and mesomorphic properties of Schiff base esters ortho-hydroxy-para-alkyloxybenzylidene-para-substituted anilines. *Molecular Crystals and Liquid Crystals*, 423**,** 73-84.

YOSHINO, K., OYAMA, S. & YONETA, M. 2008. Structural, optical and electrical characterization of undoped ZnMgO film grown by spray pyrolysis method. *Journal of Materials Science: Materials in Electronics*, 19**,** 203-209.